optica

Tunable unidirectional surface plasmon polaritons at the interface between gyrotropic and isotropic conductors

Yi Liang,[1,2] Samaneh Pakniyat,[3] Yinxiao Xiang,[1] Jun Chen,[4] Fan Shi,[1,5] George W. Hanson,[3] and Cheng Cen[1,*]

[1]Department of Physics and Astronomy, West Virginia University, Morgantown, West Virginia 26506, USA
[2]Guangxi Key Lab for Relativistic Astrophysics, Center on Nanoenergy Research, School of Physical Science and Technology, Guangxi University, Nanning, Guangxi 530004, China
[3]Department of Electrical Engineering, University of Wisconsin-Milwaukee, Milwaukee, Wisconsin 53211, USA
[4]Department of Electrical and Computer Engineering and Peterson Institute of NanoScience and Engineering, University of Pittsburgh, Pittsburgh, Pennsylvania 15261, USA
[5]Key Laboratory of Computer Vision and System of Ministry of Education, Tianjin University of Technology, Tianjin 300384, China
*Corresponding author: cheng.cen@mail.wvu.edu

Received 16 March 2021; revised 31 May 2021; accepted 31 May 2021 (Doc. ID 425290); published 24 June 2021

Unidirectionally propagated electromagnetic waves are rare in nature but heavily sought after due to their potential applications in backscatter-free optical information processing setups. It was theoretically shown that the distinct bulk optical band topologies of a gyrotropic metal and an isotropic metal can enable topologically protected unidirectional surface plasmon polaritons (SPPs) at their interface. Here, we experimentally identify such interfacial modes at terahertz frequencies. Launching the interfacial SPPs via a tailored grating coupler, the far-field spectroscopy data obtained reveals strongly nonreciprocal SPP dispersions that are highly consistent with the theoretical predictions. The directionality of the interfacial SPPs studied here is flexibly tunable by either varying the external field or adjusting the metallic characteristics of the bulk materials. The experimental realization of actively tunable unidirectional SPPs sets the foundation for developing nanophotonic information processing devices based on topologically protected interfacial waves.

https://doi.org/10.1364/OPTICA.425290

1. INTRODUCTION

Through the coupling with surface plasmon polaritons (SPPs), it is possible to confine light at the nanoscale [1–4]. While the excitation of SPPs with tailored directionalities can be achieved using various metacoupler designs [5], the propagation of SPPs in solid state systems is usually reciprocal [6], which means that a forward-traveling SPP wave can be easily backscattered by disorders. Since such backscattering is detrimental for SPP-based information processing applications, the development of nonreciprocal plasmonic platforms [7–20] that enforce unidirectional SPP propagations is of great importance. For a typical metal-dielectric plasmonic interface, when the metallic medium is gyrotropic, several earlier theoretical works have predicted the existence of frequency windows in which SPPs travel unidirectionally [21–27]. However, more recent investigations revealed a thermodynamic paradox [28,29] associated with such prediction. When considering the nonlocal effects present in realistic materials, there are no longer any strictly unidirectional frequency ranges, even in lossless systems. Theoretically, the unidirectionality of many classes of SPPs, including conventional surface magnetoplasmons, is rooted in a nonphysical flat dispersion asymptote at large wavenumbers. This kind of SPP would become bidirectional in the presence of nonlocal effects.

In order to find alternative interfaces that can support truly unidirectional SPPs, less common plasmonic material combinations need to be considered. Interestingly, it is also possible to excite SPPs at interfaces formed between two metals, given one of them is gyrotropic. At such metal-metal interfaces [23,25,30,31], not only are strictly unidirectional frequency windows present without any thermodynamic paradox [29], the unidirectionality of SPPs in these frequency windows is further protected by the topology of the bulk optical band structure [32–36]. The unidirectionality of such topological SPPs arises from a bias-induced asymmetry, and thus it is preserved when nonlocal effects are present. To experimentally demonstrate this effect, in this work we excite and characterize terahertz (THz) surface magnetoplasmons at a grating-coupled gyrotropic-metal/isotropic-metal interface at low temperatures. The theoretically predicted nonreciprocal SPP dispersions are clearly observed. This system also allows active control over both the SPP directionality and frequency with weak magnetic fields. To bridge our work with future applications, we also discuss how

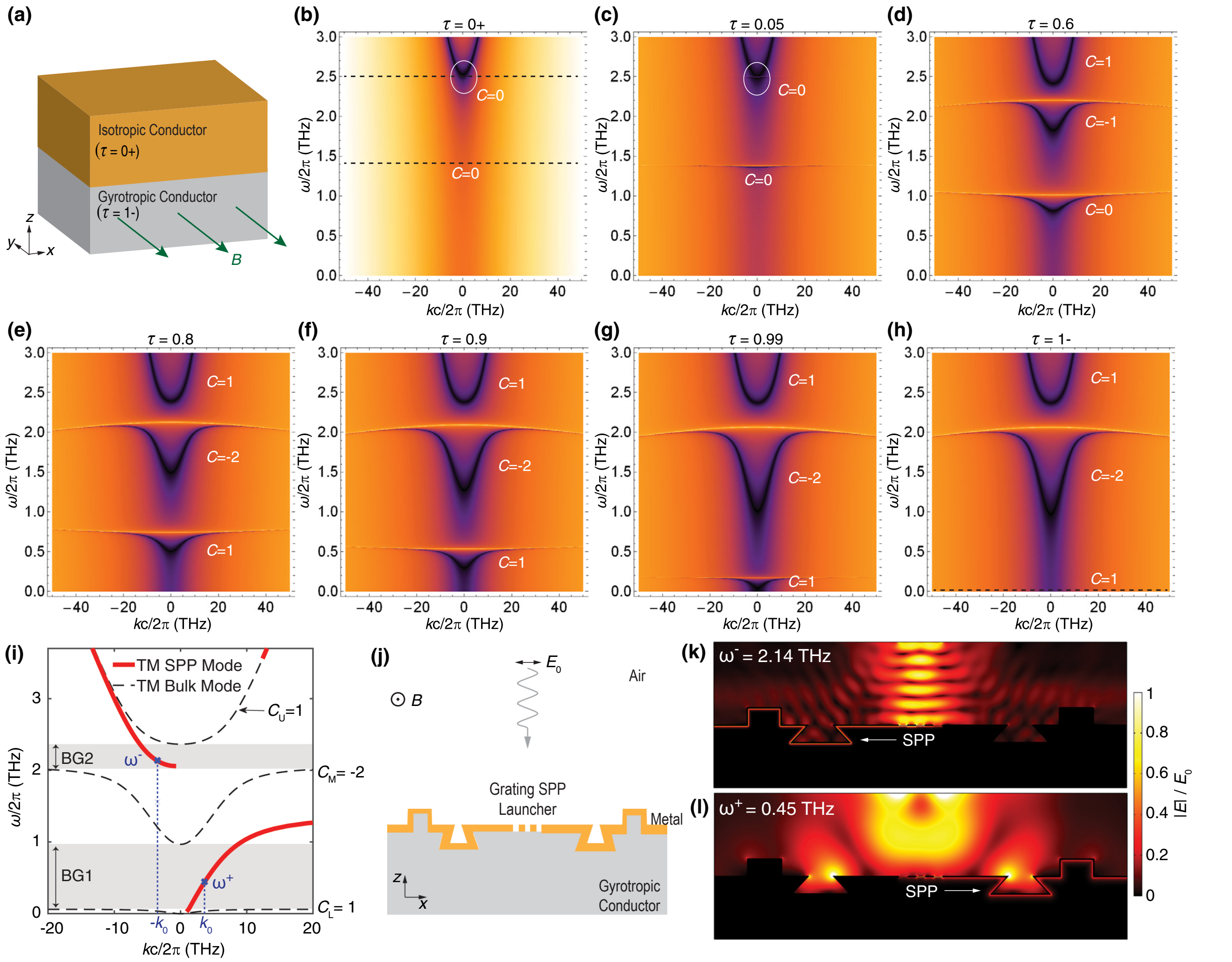

Fig. 1. Topologically protected unidirectional SPPs. (A) Schematic of a gyrotropic/isotropic conductor interface. (B)–(H) Evolution of the TM bulk band structure as a topologically trivial regular Drude metal ($\tau = 0$) is continuously transformed into a nontrivial gyrotropic conductor ($\tau = 1$). The band dispersions are visualized by plotting $\log|\varepsilon_{\mathrm{eff}}(k, \omega)\omega^2 - k^2c^2|$. Parameters used are $\omega_p/2\pi = 6\,\mathrm{THz}$, $\omega_c/2\pi = 1.4\,\mathrm{THz}$, $\omega_m/2\pi = 10\,\mathrm{THz}$, and $k_{\max}c/2\pi = 100\,\mathrm{THz}$. (I) Topologically protected unidirectional SPPs (red) emerging from the bulk gaps. (K) and (L) Simulated electric field intensities for the sample structure illustrated in (J). The size of the simulation area is 2 mm × 0.7 mm. The grating period used for SPP launching is $d = 2\pi/k_0 = 84\,\mu\mathrm{m}$.

the nonreciprocal SPP propagation is affected by practical material characteristics.

2. THEORETICAL BACKGROUND

We first introduce the basic concepts of the topologically protected interfacial SPPs studied here by considering a lossless heterostructure formed from a gyrotropic conductor that is biased by $\vec{B} = B\hat{y}$ and a regular Drude metal (Fig. 1(A)). The permittivity of the isotropic metal is a scaler ($\varepsilon_m < 0$), and the permittivity tensor of the gyrotropic conductor can be expressed as

$$\boldsymbol{\varepsilon} = \begin{pmatrix} \varepsilon_t & 0 & i\varepsilon_g \\ 0 & \varepsilon_a & 0 \\ -i\varepsilon_g & 0 & \varepsilon_t \end{pmatrix}. \tag{1}$$

In a continuous medium, due to the behavior of the Hamiltonian at infinite momentum in the 2D planar momentum space, the usual assumption of a local material model can lead to noninteger Chern numbers [32,33]. Here, in order for the isotropic metal and the gyrotropic conductor to share a common bandgap and have Chern numbers that are meaning for the bulk-edge correspondence, we use an interpolated material model to calculate the dispersion, which uses a parameter $\tau \in [0, 1]$ to represent a continuous transition between the isotropic ($\tau \to 0+$) and gyrotropic ($\tau \to 1-$) limits. Thus, the permittivity elements are defined as

$$\begin{aligned}
\varepsilon_t(k,\omega) &= \varepsilon_\infty - \tau\left(\frac{{\omega_p}^2}{\omega^2 - {\omega_c}^2}\right)\left(\frac{1}{1 + k^2/k_{\max}^2}\right) - (1-\tau)\left(\frac{{\omega_m}^2}{\omega^2}\right),\\
\varepsilon_a(k,\omega) &= \varepsilon_\infty - \tau\frac{{\omega_p}^2}{\omega^2}\left(\frac{1}{1 + k^2/k_{\max}^2}\right) - (1-\tau)\left(\frac{{\omega_m}^2}{\omega^2}\right),\\
\varepsilon_g(k,\omega) &= -\tau\left(\frac{{\omega_p}^2\omega_c}{\omega(\omega^2 - {\omega_c}^2)}\right)\left(\frac{1}{1 + k^2/k_{\max}^2}\right),
\end{aligned} \tag{2}$$

where ε_∞ is the infinite frequency permittivity, ω_p and ω_m are the plasma frequencies of the two materials, and ω_c is the cyclotron frequency. In Eq. (2), a spatial frequency cutoff k_{max} is introduced following the method in Ref [32,33]. This value is chosen to be large enough ($>100\omega_p/c$) such that its effect is only significant at the limit of $k \to \infty$. At small or moderate momentums, the electromagnetic response is very similar to a local model with $k_{max} \to \infty$. It should be noted that a hydrodynamic model would be more accurate than the spatial cutoff model at large wavenumber, but for the low-wavenumber SPPs considered here, the spatial cutoff model is expected to provide accurate results.

Inside the bulk materials, plane waves propagating perpendicular to the field include both TE and TM modes. It can be shown that the TE modes are all topologically trivial and thus will not be discussed further. The TM bulk modes, on the other hand, follow the dispersion relation

$$k_B^2 = \varepsilon_{\mathrm{eff}}\left(\frac{\omega}{c}\right)^2, \tag{3}$$

where $\varepsilon_{\mathrm{eff}} = ({\varepsilon_t}^2 - {\varepsilon_g}^2)/\varepsilon_t$ is the effective permittivity for the field-orthogonal polarizations. Equation (3) characterizes three bulk bands [upper (U), middle (M), and lower (L)] that are separated by two bandgaps (BG1 and BG2) (Figs. 1(B)–1(H)). At the limits of $\tau \to 0$ and $\tau \to 1$, some of the bands are dark modes decoupled from the electromagnetic field (dashed lines in Figs. 1(B) and 1(H)).

In a continuous medium, by mapping the unbounded $\vec{k}$-space onto the Riemann sphere [33], it is possible to assign an integer Chern number to each bulk band that is separated from the others by a complete bandgap [37–39]. At the limit of $\tau \to 0$ (isotropic metal), the Chern numbers of the three bands are all zero, while for $\tau \to 1$ (gyrotropic conductor), the nontrivial Chern numbers are found to be [40] $C_U = 1$, $C_M = -2$, and $C_L = 1$. As τ varies from 0 to 1, the band structure changes are shown in Figs. 1(B)–1(H). Two topological phase transitions occur during this process, each associated with changes in the Chern numbers. The first transition, marked by the opening of BG2 at $k = 0$, takes place near $\tau \to 0$. The second transition occurs between $\tau = 0.6$ and $\tau = 0.8$, where C_M and C_L abruptly change from (1,0) to $(-2, 1)$. Similar to what is discussed in Ref [32,33], this transition is driven by the closing and reopening of BG1 at very large k.

The distinct topologies at the two sides of the interface mandates the formation of in-gap surface states. The sum of the Chern numbers for each band below the gap (gap Chern number) indicates the number of topologically protected surface modes crossing the gap. The gap Chern numbers of BG1 and BG2 are 1 and -1. Thus, two in-gap unidirectional SPP branches, one in each gap, are present in this system (Fig. 1(I), red). The SPP dispersion equation derived based on the nonlocal model [Eq. (2)] is shown in the supporting materials. For relatively small k values (e.g., those accessible in experiments), the SPP dispersion can be approximated by the simpler expression obtained at the local limit $k_{max} \to \infty$:

$$\frac{\sqrt{k_{\mathrm{SPP}}^2 - k_0^2\varepsilon_m}}{\varepsilon_m} + \frac{\sqrt{k_{\mathrm{SPP}}^2 - k_0^2\varepsilon_{\mathrm{eff}}}}{\varepsilon_{\mathrm{eff}}} = \frac{\varepsilon_g}{\varepsilon_t\varepsilon_{\mathrm{eff}}}k_{\mathrm{SPP}}. \tag{4}$$

Within the bulk gaps, the SPP unidirectionality is topologically protected and therefore immune to backscattering. One example of such effect is shown in Figs. 1(J)–1(L). In this setup (Fig. 1(J)), the grating at the center is designed to be in resonance with two in-gap SPP modes traveling in opposite directions: (k_0, ω^+) and $(-k_0, \omega^-)$, which are indicated by blue dots in Fig. 1(I). When excited by light of frequency ω^-, only the left-traveling mode is allowed at the interface (Fig. 1(K)). In comparison, when tuning the light frequency to ω^+, the SPP wave launched only travels toward the right (Fig. 1(I)). In both cases, the propagating SPP experiences no scattering at the sharp bending points placed along its paths. We note that SPP modes outside the bulk gaps can also be unidirectional within selected frequency ranges (Fig. 1(I)), though these out-of-gap unidirectional waves are not topologically protected and subject to scattering with the bulk modes.

3. EXPERIMENTAL RESULTS

To realize the gyrotropic/isotropic heterostructure in experiment, Au films are deposited on the surfaces of undoped InSb single crystals. Here, magnetized InSb serves as the gyrotropic conducting medium. Its high electron mobility and small effective mass allows the generation of strong magneto-optical effects with weak magnetic fields [41–51]. Grating structures are fabricated in the Au layer to provide the momentum matching and allow the excitation of SPPs from free-space light (Fig. 2(A)). In experiment, the magnetic field is kept parallel to the grating grooves and the incident polarization is perpendicular to the grooves. The SPPs launched need to satisfy the momentum conservation rule

$$k_{\mathrm{SPP}} = \frac{\omega}{c}\sin\theta \pm \frac{2\pi}{d}, \tag{5}$$

where d is the grating constant and θ is the incident angle. Equation (5) traces out two parallel straight lines in the (k, ω) plane. The intersections of these two lines with the SPP dispersion curve [Eq. (4)] determine the SPP modes that can be excited (Figs. 2(F)–2(H)). Signatures of the SPPs are detected in a reflection geometry using the THz time-domain spectroscopy (THz-TDS) method.

Figures 2(C) and 2(D) compare the 50 K THz reflectance ($r = E_{\mathrm{reflection}}/E_{\mathrm{incidence}}$) measured with a normal incidence ($\theta = 0$) on the two different halves of the same sample: one with a bare surface (Fig. 2(C)) and the other with an Au grating structure on top (Fig. 2(D)). In this InSb sample, the electron mobility maximizes at 50 K ($\mu = 22\ \mathrm{m^2/Vs}$), where the carrier density $n = 1 \times 10^{20}\ \mathrm{m^{-3}}$ and the carrier scattering rate $\Gamma = e/\mu m^* = 5.7 \times 10^{11}\ \mathrm{s^{-1}}$ ($m^* = 0.014 m_0$ is the effective electron mass) are relatively low, corresponding to an effective plasma frequency of $\omega_p{}^* = \omega_p/\sqrt{\varepsilon_\infty} = \sqrt{ne^2/m^*\varepsilon_\infty\varepsilon_0} \approx 0.2\ \mathrm{THz}$. On the unpatterned region, free-space light cannot directly couple to the SPPs, and the most noticeable feature observed is the field-induced reflectance modulations near $\omega_c = eB/m^*$, which blueshift as the magnetic field increases (Fig. 2(C)). In comparison, the reflectance peaks associated with SPPs, as well as their anti-crossing with the cyclotron resonances, are clearly visible in the data acquired on the region covered by Au grating (Fig. 2(D)).

At zero field, since Eqs. (4) and (5) are both symmetric in the k-space, a pair of SPP modes are simultaneously generated, which travel in opposite directions but have the same frequency and propagation length (Fig. 2(F)). This pair of SPPs are represented by a single peak in the reflectance spectrum (Fig. 2(D)). Applying a nonzero field, the SPP branches below ω_c are no longer k-symmetric (Figs. 2(G) and 2(H)). When $B = 0.45$ T, ω_c overlaps with the SPP frequency and causes the SPP propagation in both directions to be significantly damped (Fig. 2(G)). When B further increases to 0.7 T, a pair of SPP modes are again excited

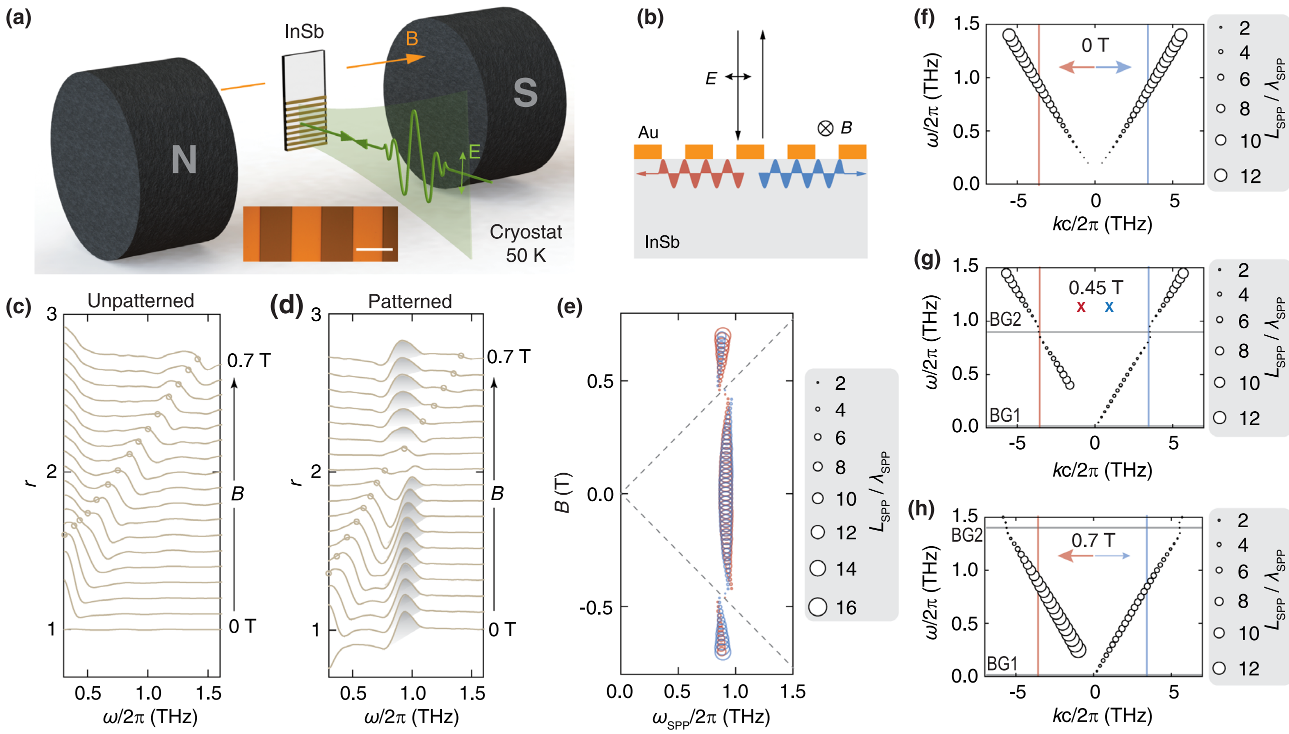

Fig. 2. Surface magnetoplasmons generated at InSb/Au interface by normal incident light. (A) Schematic of the measurement configuration. The inset shows the optical image of the Au grating (scale bar represents 50 μm). (B) Side view of the measurement geometry. (C) and (D) Field-dependent reflectance spectra obtained on the unpatterned half of (C) the sample and (D) the patterned half at 50 K. The cyclotron frequencies are marked by small circles, and the SPP peaks are highlighted in grey. (E) Calculated SPP resonance frequencies for different fields. Left-traveling SPPs are plotted using red bubbles, and right-traveling SPPs are plotted with blue bubbles. The bubble size represents the SPP propagation lengths normalized by the wavelengths (L_{SPP}/λ_{SPP}). (F)–(H) SPP dispersions for three different magnetic fields. The red and blue lines show the grating resonance conditions for the left-traveling (red) and right-traveling (blue) SPPs under normal incidence. In (G) and (H), the two field-induced bulk gaps are marked by grey shaded areas.

with approximately the same frequency, though the left-traveling wave has a substantially longer propagation length compared to the right-traveling one (Fig. 2(H)). Figure 2(E) plots the SPP resonance frequencies calculated for different field values, which are highly consistent with the experimental observations. In general, at 50 K, left-traveling and right-traveling SPPs excited by the normal-incidence light are degenerate in energy. They are either generated in pairs or both suppressed when varying the magnetic field.

The situation is different when $\theta \neq 0$. As shown in Fig. 3(A), mounting the sample next to a silver mirror and forming a normal angle between the two surfaces, a THz beam focused on the sample-mirror boundary hits the two surfaces consecutively with an angle and gets retroreflected in the end. One complication associated with this setup is that the reflectance measured is a combined result of $\theta = \pm 45°$ incidences: θ for the beam portion that hits the sample first is 45°, whereas the other portion that gets reflected by the mirror first hits the sample surface with a -−45° angle. The sample reflectances corresponding to the two incident angles are linked by symmetry. For simplicity, we first focus on the case of $\theta = 45°$, and the other case of $\theta = -45°$ can be directly inferred by the relation of $r(-\theta, B) = r(\theta, -B)$.

For $\theta = 45°$, Eq. (5) results in two slanted lines in the (k, ω) plane that are no longer k-symmetric (solid lines, Figs. 3(E)–3(G)). Such asymmetry lifts the energy degeneracy between the SPPs excited in opposite directions and thus allows them to be distinguished experimentally as shown by the two separate SPP peaks in Fig. 3(C). As the external field varies, the cyclotron resonance intercepts with the left- and right-traveling SPP modes one at a time (Figs. 3(C) and 3(D)), allowing them to be manipulated individually. This effect produces multiple magnetic field windows in which the SPP launched is unidirectional (Fig. 3(D), green shaded regions). Near $B = 0.35$ T, the left-traveling mode is suppressed by the field, and only the right-traveling SPP is allowed at the interface (Fig. 3(F)). The situation is reversed near $B = 0.57$ T, where only the left-traveling SPP is allowed (Fig. 3(G)).

Comparing the SPP dispersions shown in Figs. 2(G), 2(H) and Fig. 3(G) to the ideal lossless case shown in Fig. 1(I), a big difference is that the SPP modes between the two bulk gaps are no longer unidirectional for magnetic fields larger than 0.4 T. Since the SPPs outside the bulk gaps are not topologically protected, their directionality is sensitive to the changes in symmetry-unrelated sample parameters. When the carrier density of InSb is low (e.g., at 50 K), the SPP dispersion between the bulk gaps is strongly affected by the surface quality of the Au film. In this work, a literature-reported Au film permittivity of $\varepsilon_m = -800 + i500$ obtained from SPP-based measurements [52,53] is found to be most consistent with our experimental observations [54]. If the bulk permittivity value ($\varepsilon_m^{\mathrm{Drude}} = -2.3 \times 10^5 + i8.6 \times 10^5$) [55] can be realized at the surface of the Au films, the SPP dispersion at the interface will become much more similar to the ideal case (Fig. S1, Supplement 1).

At higher temperatures, thermal activation causes the electron density in InSb to rise, changing the bulk and surface band structures significantly (Fig. S2 of Supplement 1, Figs. 4(C), 4(G), and 4(K)). Figures 4(A), 4(E), and 4(I) compare the normal-incidence reflectances measured at 50 K, 180 K ($n = 4.5 \times 10^{20}$ m^{-3},

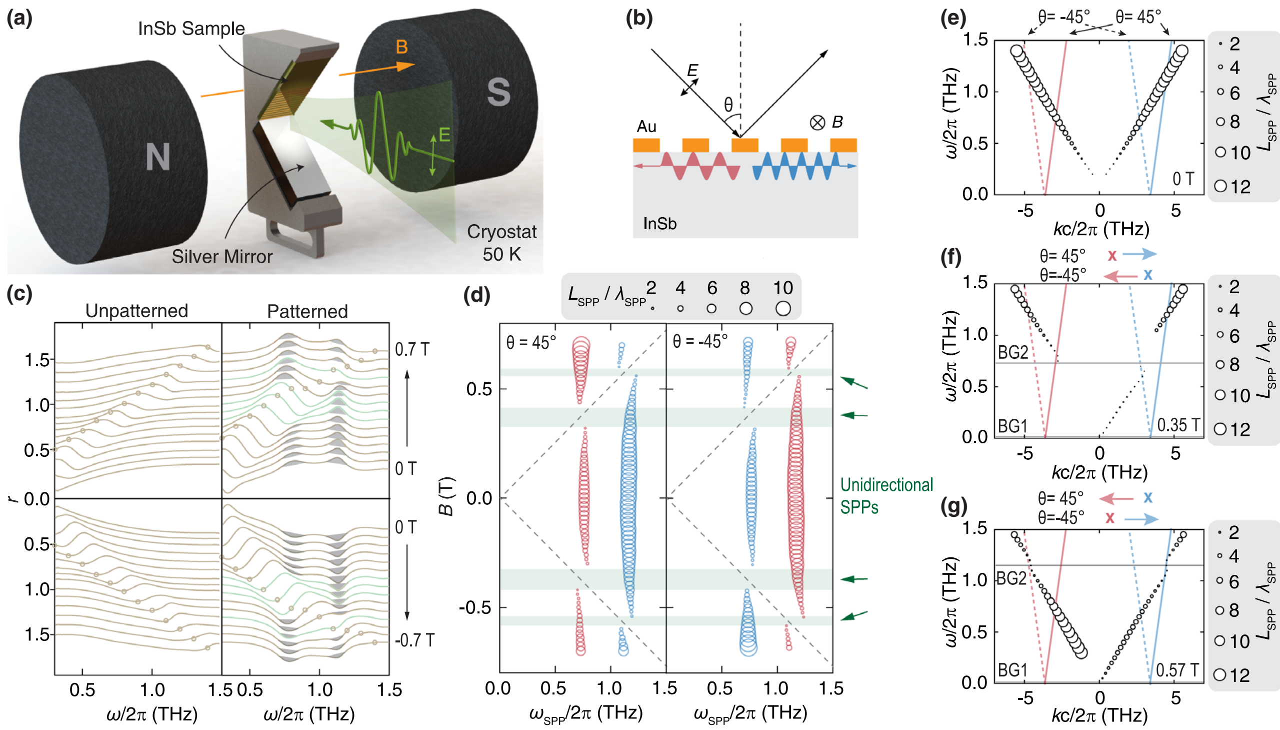

Fig. 3. Unidirectional SPPs generated by light with a nonzero incidence angle. (A) Schematic of the measurement configuration. (B) Side view of the measurement geometry. (C) Field-dependent reflectance spectra measured on unpatterned and patterned sample halves at 50 K. Curves corresponding to unidirectional SPP excitations are highlighted in green. (D) SPP resonance frequencies calculated for the two incidence angles of ±45°. The field ranges corresponding to unidirectional SPPs are marked in green. (E)–(G) SPP dispersions for three field values.

$\omega_p^* = 0.4$ THz, $\mu = 11\ \mathrm{m^2/Vs}$), and 250 K ($n = 4.5 \times 10^{21}\ \mathrm{m^{-3}}$, $\omega_p^* = 1.1$ THz, $\mu = 6\ \mathrm{m^2/Vs}$). Here, instead of extracting the absolute reflectance $r(B)$, which requires a reference sample to be repeatedly positioned to precisely match the different sample positions at varied temperatures, the reflectance data is processed in a self-referenced manner. That is, the raw reflectance signal detected at a nonzero field is divided by its zero-field value ($r(B)/r(0)$), which captures the field-induced reflectance change without the need for separate reference measurements.

On bare InSb (Figs. 4(A), 4(E), 4(I), top), the most outstanding features of $r(B)/r(0)$ are a peak near ω_p^* and a plateau that broadens as B increases. The right edge of the plateau traces the bottom of the upper bulk band, which approximates ω_c when $\omega_p^* \ll \omega_c$. With the Au grating, the broadening of the plateau appears to be intercepted at the zero-field SPP frequency (Figs. 4(A), 4(E), 4(I), bottom), and the peak near the plateau edge indicates the SPP frequency under the influence of the nonzero field. The single SPP peak detected at $\theta = 0°$ splits into two when θ changes to ±45° (Figs. 4(B), 4(F), and 4(J)). At 50 K, the higher frequency peak represents the forward-propagating (as compared to the in-plane direction of the incidence light) modes generated by the ±45° incidences [$\omega_{\mathrm{SPP}}^{(f)}(\pm 45°)$], and the lower frequency peak represents the counterpropagating modes [$\omega_{\mathrm{SPP}}^{(c)}(\pm 45°)$] (Fig. 4(C)). At 180 K and 250 K, the two peaks come from the forward-traveling mode generated by the +45° incidence [$\omega_{\mathrm{SPP}}^{(f)}(45°)$] and the counter-traveling mode generated by the −45° incidence [$\omega_{\mathrm{SPP}}^{(c)}(-45°)$], both modes can only propagate toward the right (Figs. 4(G) and 4(K)). As shown in Figs. 4(D), 4(H), and 4(L), the raised ω_p^* makes the bulk gaps (grey shaded areas) and the unidirectional magnetic field windows (green shaded areas) both more sizable at higher temperatures. As a result, it is much easier to generate topologically protected unidirectional SPPs at 250 K (modes in regions where the two shaded areas overlap). Nonetheless, due to the reduced electron mobility, the propagation lengths of these modes are short.

An important feature of the SPPs at the gyrotropic/isotropic interface is that they are nonreciprocal. Since the operation of $B \to -B$ mirrors the k-asymmetric SPP dispersion curve with respect to $k = 0$, for any single θ value, flipping the field orientation will lead to the excitation of different SPP modes. The $\theta = \pm 45°$ dual incident angle setup weakens such effect significantly, but due to the nonperfect beam shape in the experiment and the weak imbalance between the two incidence angles, the nonreciprocal SPP excitations can still be detected. The insets of Figs. 4(B) and 4(F) plot the differences between the data measured at ±0.7 T. The absolute value of the difference signal maximizes near the two SPP resonances, but the sign of the signal changes in between, indicating a spectral weight shift between the two modes as the field orientation flips. In comparison, the ±0.7 T signals measured on the bare InSb surface are almost identical (Fig. S3, Supplement 1). Notably, the sign of the difference signal also flips when raising the temperature from 50 K to 180 K. This observation is consistent with the different SPP asymmetry found at the two temperatures (Figs. 4(C) and 4(G)). At 50 K, the $k < 0$ SPP branch below BG2 is stronger than the $k > 0$ branch in the sense that it has much longer propagation lengths. At 180 K, the $k > 0$ branch becomes the stronger one since the $k < 0$ branch is no longer present.

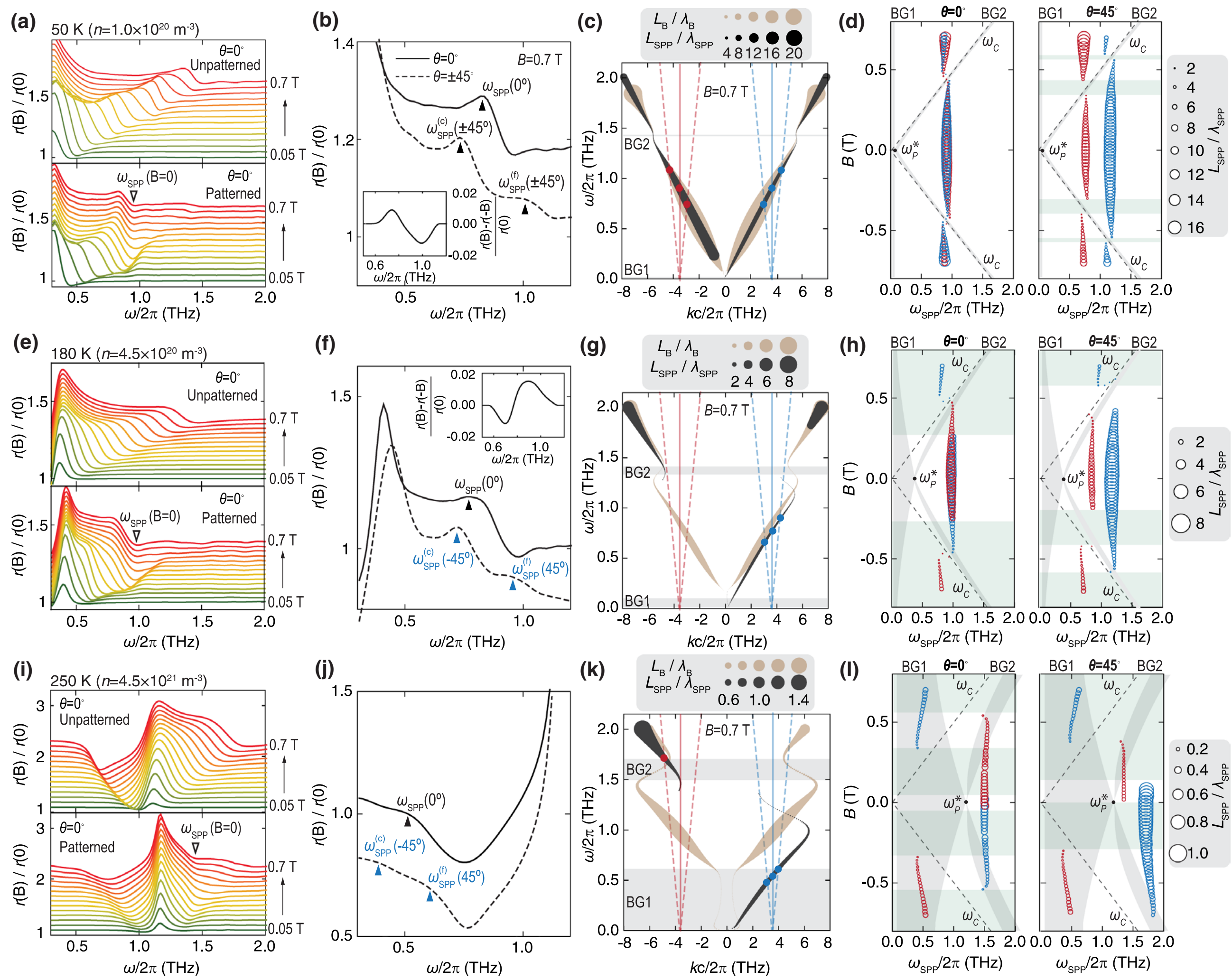

Fig. 4. Nonreciprocal SPP responses and temperature dependence. (A) Field-induced reflectance changes on bare (top) and patterned (bottom) sample regions at 50 K. (B) Field-induced reflectance changes at 0.7 T with normal (solid curve) and ±45° (dashed curve) incidences. The inset shows the difference between the data obtained at $B = \pm 0.7$ T. (C) Dispersion relations of bulk modes (brown) and SPPs (black) at $B = 0.7$ T. (D) SPP resonance frequencies calculated for $\theta = 0^\circ$ and 45°. (E)–(L) are similar to (A)–(D) but for higher temperatures of 180 K and 250 K. In (D), (H), and (L), bulk gaps are marked by grey and unidirectional field windows are marked by green. The unidirectionality of the modes residing in the overlapping regions is topologically protected. The modes residing inside the green region but outside the grey region are also unidirectional but are not topologically protected.

4. DISCUSSION

In summary, we have successfully excited unidirectional THz surface magnetoplasmons at the gyrotropic-metal/isotropic-metal interface formed between magnetized InSb single crystal and Au film. Varying the external magnetic field, the directionality of the interfacial SPPs that can propagate is flexibly tunable. Controlling the carrier density in InSb, we are able to change the bulk gap sizes and observe different nonreciprocal interface dispersions. These results demonstrate the possibility of realizing topologically protected active nonreciprocal plasmonics at THz frequencies using heterostructures formed from materials with distinct optical band topologies.

For practical applications, we find it desirable to work with a gyrotropic conductor with a relatively larger effective plasma frequency ω_p^*. On one hand, it helps widen the bulk optical bandgaps and thus extend the bandwidth of the topologically protected interfacial SPPs. On the other, it makes the unidirectionality of the out-of-gap SPPs, which are not topologically protected, more robust against the parameter fluctuations in the isotropic metal layer. Since a larger ω_p^* also means that a larger magnetic field is required to generate a sizable gyrotropic permittivity element, there exists an optimal window of ω_p^* for unidirectional SPP applications, the value of which is determined by the effective carrier mass in the gyrotropic medium. For InSb, such optimal ω_p^* window occurs when the carrier density is at the level of 10^{21}–10^{22} m^{-3}. With such electron densities, however, the propagation lengths of the unidirectional interfacial SPPs are significantly limited by both the interface quality of the deposited Au film and the electron mobility in InSb. The interfacial properties of Au films are often affected by the presence of an additional adhesion layer (e.g., Ti as used in this work). By depositing directly on substrates cooled to cryogenic temperatures without an adhesion layer [56] or using unconventional adhesion materials [57,58], ultrasmooth Au films can be fabricated with greatly improved plasmonic performances. For undoped InSb single crystals as used in this experiment, the $10^{21} - 10^{22}$ m^{-3} electron density values are found near room temperature. Since in this case the dominating mobility limiting factor is the carrier scattering with optical phonons [59–61], there is little room for improvement. Alternatively, similar electron densities can also be found in lightly doped n-type InSb near liquid nitrogen temperature but with much higher mobility values [61,62]. Through these future material optimizations, the long-living unidirectional SPPs that can be excited at gyrotropic-metal/isotropic-metal interfaces will provide a unique venue for exploring nonreciprocal plasmonic functionalities on chip.

Funding. National Science Foundation (1741673); National Natural Science Foundation of China (11604058); Natural Science Foundation of Guangxi Province (2020GXNSFAA297041).

Acknowledgment. Y.L., C.C., and F. S. performed the THz-TDS measurements. S. P., Y. X., and G. H. carried out the theoretical and numerical calculations. J. C. performed the sample fabrications. C.C. and G.H. conceived and organized the study. Y. L. and C. C. analyzed the data and wrote the paper. All authors discussed the results and commented on the paper.

Disclosures. The authors declare no conflicts of interest.

Data availability. Data underlying the results presented in this paper are not publicly available at this time but may be obtained from the authors upon reasonable request.

Supplemental document. See Supplement 1 for supporting content.

REFERENCES

1. S. A. Maier and H. A. Atwater, "Plasmonics: localization and guiding of electromagnetic energy in metal/dielectric structures," J. Appl. Phys. **98**, 011101 (2005).
2. E. Ozbay, "Plasmonics: merging photonics and electronics at nanoscale dimensions," Science **311**, 189–193 (2006).
3. W. L. Barnes, A. Dereux, and T. W. Ebbesen, "Surface plasmon subwavelength optics," Nature **424**, 824–830 (2003).
4. D. K. Gramotnev and S. I. Bozhevolnyi, "Plasmonics beyond the diffraction limit," Nature Photonics **4**, 83–91 (2010).
5. F. Ding and S. I. Bozhevolnyi, "A review of unidirectional surface plasmon polariton metacouplers," IEEE J. Sel. Top. Quantum Electron. **25**, 1–11 (2019).
6. D. Jalas, A. Petrov, M. Eich, W. Freude, S. Fan, Z. Yu, R. Baets, M. Popović, A. Melloni, J. D. Joannopoulos, M. Vanwolleghem, C. R. Doerr, and H. Renner, "What is — and what is not — an optical isolator," Nat. Photonics **7**, 579–582 (2013).
7. W. Zhang and X. Zhang, "Backscattering-immune computing of spatial differentiation by nonreciprocal plasmonics," Phys. Rev. Appl. **11**, 054033 (2019).
8. J. Y. Chin, T. Steinle, T. Wehlus, D. Dregely, T. Weiss, V. I. Belotelov, B. Stritzker, and H. Giessen, "Nonreciprocal plasmonics enables giant enhancement of thin-film Faraday rotation," Nat. Commun. **4**, 1599 (2013).
9. D. Frese, Q. Wei, Y. Wang, L. Huang, and T. Zentgraf, "Nonreciprocal asymmetric polarization encryption by layered plasmonic metasurfaces," Nano Lett. **19**, 3976–3980 (2019).
10. A. R. Davoyan and N. Engheta, "Nanoscale plasmonic circulator," New J. Phys. **15**, 083054 (2013).
11. A. Davoyan and N. Engheta, "Electrically controlled one-way photon flow in plasmonic nanostructures," Nat. Commun. **5**, 5250 (2014).
12. V. V. Temnov, G. Armelles, U. Woggon, D. Guzatov, A. Cebollada, A. Garcia-Martin, J.-M. Garcia-Martin, T. Thomay, A. Leitenstorfer, and R. Bratschitsch, "Active magneto-plasmonics in hybrid metal–ferromagnet structures," Nat. Photonics **4**, 107–111 (2010).
13. Z. Yu, G. Veronis, Z. Wang, and S. Fan, "One-way electromagnetic waveguide formed at the interface between a plasmonic metal under a static magnetic field and a photonic crystal," Phys. Rev. Lett. **100**, 023902 (2008).
14. D. Correas-Serrano and J. S. Gomez-Diaz, "Nonreciprocal and collimated surface plasmons in drift-biased graphene metasurfaces," Phys. Rev. B **100**, 081410 (2019).
15. D. Correas-Serrano, A. Alù, and J. S. Gomez-Diaz, "Magnetic-free nonreciprocal photonic platform based on time-modulated graphene capacitors," Phys. Rev. B **98**, 165428 (2018).
16. V. I. Belotelov, L. E. Kreilkamp, I. A. Akimov, A. N. Kalish, D. A. Bykov, S. Kasture, V. J. Yallapragada, A. Venu Gopal, A. M. Grishin, S. I. Khartsev, M. Nur-E-Alam, M. Vasiliev, L. L. Doskolovich, D. R. Yakovlev, K. Alameh, A. K. Zvezdin, and M. Bayer, "Plasmon-mediated magneto-optical transparency," Nat. Commun. **4**, 2128 (2013).
17. D. Wang, B. Yang, W. Gao, H. Jia, Q. Yang, X. Chen, M. Wei, C. Liu, M. Navarro-Cía, J. Han, W. Zhang, and S. Zhang, "Photonic Weyl points due to broken time-reversal symmetry in magnetized semiconductor," Nat. Phys. **15**, 1150–1155 (2019).
18. K. Shastri, M. I. Abdelrahman, and F. Monticone, "Nonreciprocal and topological plasmonics," Photonics **8**, 133 (2021).
19. S. A. H. Gangaraj, A. Nemilentsau, and G. W. Hanson, "The effects of three-dimensional defects on one-way surface plasmon propagation for photonic topological insulators comprised of continuum media," Sci. Rep. **6**, 30055 (2016).
20. S. A. H. Gangaraj and F. Monticone, "Topological waveguiding near an exceptional point: defect-immune, slow-light, and loss-immune propagation," Phys. Rev. Lett. **121**, 093901 (2018).
21. J. J. Brion, R. F. Wallis, A. Hartstein, and E. Burstein, "Theory of surface magnetoplasmons in semiconductors," Phys. Rev. Lett. **28**, 1455–1458 (1972).
22. L. Shen, Y. You, Z. Wang, and X. Deng, "Backscattering-immune one-way surface magnetoplasmons at terahertz frequencies," Opt. Express **23**, 950–962 (2015).
23. S. A. H. Gangaraj and F. Monticone, "Topologically-protected one-way leaky waves in nonreciprocal plasmonic structures," J. Phys. Condens. Matter **30**, 104002 (2018).
24. B. Hu, Q. J. Wang, and Y. Zhang, "Broadly tunable one-way terahertz plasmonic waveguide based on nonreciprocal surface magneto plasmons," Opt. Lett. **37**, 1895–1897 (2012).
25. S. A. H. Gangaraj, G. W. Hanson, M. G. Silveirinha, K. Shastri, M. Antezza, and F. Monticone, "Unidirectional and diffractionless surface plasmon polaritons on three-dimensional nonreciprocal plasmonic platforms," Phys. Rev. B **99**, 245414 (2019).
26. K. L. Tsakmakidis, L. Shen, S. A. Schulz, X. Zheng, J. Upham, X. Deng, H. Altug, A. F. Vakakis, and R. W. Boyd, "Breaking Lorentz reciprocity to overcome the time-bandwidth limit in physics and engineering," Science **356**, 1260–1264 (2017).
27. S. A. Mann, D. L. Sounas, and A. Alù, "Nonreciprocal cavities and the time–bandwidth limit," Optica **6**, 104–110 (2019).
28. S. Buddhiraju, Y. Shi, A. Song, C. Wojcik, M. Minkov, I. A. D. Williamson, A. Dutt, and S. Fan, "Absence of unidirectionally propagating surface plasmon-polaritons at nonreciprocal metal-dielectric interfaces," Nat. Commun. **11**, 674 (2020).
29. S. A. H. Gangaraj and F. Monticone, "Do truly unidirectional surface plasmon-polaritons exist?" Optica **6**, 1158–1165 (2019).
30. S. R. Seshadri, "Excitation of surface waves on a perfectly conducting screen covered with anisotropic plasma," IRE Trans. Microw. Theory Tech. **10**, 573–578 (1962).
31. S. Pakniyat, A. M. Holmes, G. W. Hanson, S. A. H. Gangaraj, M. Antezza, M. G. Silveirinha, S. Jam, and F. Monticone, "Non-reciprocal, robust surface plasmon polaritons on gyrotropic interfaces," IEEE Trans. Antennas Propag. **68**, 3718–3729 (2020).
32. M. G. Silveirinha, "Bulk-edge correspondence for topological photonic continua," Phys. Rev. B **94**, 205105 (2016).
33. M. G. Silveirinha, "Chern invariants for continuous media," Phys. Rev. B **92**, 125153 (2015).
34. M. T. Van and J. Zubin, "Unidirectional Maxwellian spin waves," Nanophotonics **8**, 1399–1416 (2019).
35. S. A. H. Gangaraj, M. G. Silveirinha, and G. W. Hanson, "Berry phase, berry connection, and chern number for a continuum bianisotropic material from a classical electromagnetics perspective," IEEE J. Multiscale Multiphys. Comput. Tech. **2**, 3–17 (2017).
36. M. G. Silveirinha, "Quantized angular momentum in topological optical systems," Nat. Commun. **10**, 349 (2019).
37. L. Lu, J. D. Joannopoulos, and M. Soljačić, "Topological photonics," Nat. Photonics **8**, 821–829 (2014).
38. S. Raghu and F. D. M. Haldane, "Analogs of quantum-Hall-effect edge states in photonic crystals," Phys. Rev. A **78**, 033834 (2008).

39. F. D. M. Haldane and S. Raghu, "Possible realization of directional optical waveguides in photonic crystals with broken time-reversal symmetry," Phys. Rev. Lett. **100**, 013904 (2008).
40. G. W. Hanson, S. Gangaraj, and A. Nemilentsau, "Notes on photonic topological insulators and scattering-protected edge states-a brief introduction," arXiv preprint arXiv:1602.02425 (2016).
41. E. D. Palik and J. K. Furdyna, "Infrared and microwave magnetoplasma effects in semiconductors," Rep. Prog. Phys. **33**, 1193–1322 (1970).
42. J. Chochol, K. Postava, M. Čada, M. Vanwolleghem, L. Halagačka, J.-F. Lampin, and J. Pištora, "Magneto-optical properties of InSb for terahertz applications," AIP Adv. **6**, 115021 (2016).
43. U. Merkt, "Surface cyclotron resonance on InSb in Voigt configuration," Phys. Rev. B **32**, 6699–6712 (1985).
44. B. Hu, Y. Zhang, and Q. J. Wang, "Surface magneto plasmons and their applications in the infrared frequencies," Nanophotonics **4**, 383–396 (2015).
45. J. Chochol, K. Postava, M. Čada, and J. Pištora, "Experimental demonstration of magnetoplasmon polariton at InSb(InAs)/dielectric interface for terahertz sensor application," Sci. Rep. **7**, 13117 (2017).
46. A. Hartstein and E. Burstein, "Observation of magnetoplasma type surface polaritons on n-InSb," Solid State Commun. **14**, 1223–1227 (1974).
47. J. Chochol, M. Mičica, K. Postava, M. Vanwolleghem, J. Lampin, M. Čada, and J. Pištora, "Demonstration of magnetoplasmon polariton at InSb/dielectric interface," in *43rd International Conference on Infrared, Millimeter, and Terahertz Waves (IRMMW-THz)* (2018), pp. 1–2.
48. A. Ritz and H. Lüth, "Experimental evidence for surface quenching of the surface plasmon on InSb(110)," Phys. Rev. Lett. **52**, 1242–1245 (1984).
49. W. E. Anderson, R. W. Alexander, and R. J. Bell, "Surface plasmons and the reflectivity of n-type InSb," Phys. Rev. Lett. **27**, 1057–1060 (1971).
50. A. Hartstein, E. Burstein, E. D. Palik, R. W. Gammon, and B. W. Henvis, "Investigation of optic-phonon—magnetoplasmon-type surface polaritons on n-InSb," Phys. Rev. B **12**, 3186–3199 (1975).
51. Y. Liang, S. Pakniyat, Y. Xiang, F. Shi, G. W. Hanson, and C. Cen, "Temperature-dependent transverse-field magneto-plasmons properties in InSb," Opt. Mater. **112**, 110831 (2021).
52. S. Pandey, S. Liu, B. Gupta, and A. Nahata, "Self-referenced measurements of the dielectric properties of metals using terahertz time-domain spectroscopy via the excitation of surface plasmon-polaritons," Photon. Res. **1**, 148–153 (2013).
53. S. Pandey, B. Gupta, A. Chanana, and A. Nahata, "Non-Drude like behaviour of metals in the terahertz spectral range," Adv. Phys. X **1**, 176–193 (2016).
54. S. Pakniyat, Y. Liang, Y. Xiang, C. Cen, J. Chen, and G. W. Hanson, "Indium antimonide—Constraints on practicality as a magneto-optical platform for topological surface plasmon polaritons," J. Appl. Phys. **128**, 183101 (2020).
55. M. A. Ordal, L. L. Long, R. J. Bell, S. E. Bell, R. R. Bell, R. W. Alexander, and C. A. Ward, "Optical properties of the metals Al, Co, Cu, Au, Fe, Pb, Ni, Pd, Pt, Ag, Ti, and W in the infrared and far infrared," Appl. Opt. **22**, 1099–1119 (1983).
56. R. Lemasters, C. Zhang, M. Manjare, W. Zhu, J. Song, S. Urazhdin, H. J. Lezec, A. Agrawal, and H. Harutyunyan, "Ultrathin wetting layer-free plasmonic gold films," ACS Photon. **6**, 2600–2606 (2019).
57. L. Leandro, R. Malureanu, N. Rozlosnik, and A. Lavrinenko, "Ultrathin, ultrasmooth gold layer on dielectrics without the use of additional metallic adhesion layers," ACS Appl. Mater. Interfaces **7**, 5797–5802 (2015).
58. D. I. Yakubovsky, Y. V. Stebunov, R. V. Kirtaev, G. A. Ermolaev, M. S. Mironov, S. M. Novikov, A. V. Arsenin, and V. S. Volkov, "Ultrathin and ultrasmooth gold films on monolayer MoS_2," Adv. Mater. Interfaces **6**, 1900196 (2019).
59. H. Ehrenreich, "Electron scattering in InSb," J. Phys. Chem. Solids **2**, 131–149 (1957).
60. C. A. Lehner, T. Tschirky, T. Ihn, W. Dietsche, J. Keller, S. Fält, and W. Wegscheider, "Limiting scattering processes in high-mobility InSb quantum wells grown on GaSb buffer systems," Phys. Rev. Mater. **2**, 054601 (2018).
61. H. J. Hrostowski, F. J. Morin, T. H. Geballe, and G. H. Wheatley, "Hall effect and conductivity of InSb," Phys. Rev. **100**, 1672–1676 (1955).
62. D. L. Rode, "Electron transport in InSb, InAs, and InP," Phys. Rev. B **3**, 3287–3299 (1971).